

## Comparative spectra and efficiencies of ions laser-accelerated forward from the front and rear surfaces of thin solid foils

J. Fuchs,<sup>1,2,3,a)</sup> Y. Sentoku,<sup>1,3</sup> E. d'Humières,<sup>2,3</sup> T. E. Cowan,<sup>1,3</sup> J. Cobble,<sup>4</sup> P. Audebert,<sup>2</sup> A. Kemp,<sup>1,3</sup> A. Nikroo,<sup>1</sup> P. Antici,<sup>2</sup> E. Brambrink,<sup>2,5</sup> A. Blazevic,<sup>5</sup> E. M. Campbell,<sup>1</sup> J. C. Fernández,<sup>4</sup> J.-C. Gauthier,<sup>2,b)</sup> M. Geissel,<sup>5</sup> M. Hegelich,<sup>4,6</sup> S. Karsch,<sup>6</sup> H. Popescu,<sup>2</sup> N. Renard-LeGalloudec,<sup>3</sup> M. Roth,<sup>5</sup> J. Schreiber,<sup>6</sup> R. Stephens,<sup>1</sup> and H. Pépin<sup>2,7</sup>

<sup>1</sup>General Atomics, San Diego, California 92121

<sup>2</sup>LULI, École Polytechnique, CNRS-CEA, UPMC, route de Saclay, 91128 Palaiseau, France

<sup>3</sup>Physics Department, MS-220, University of Nevada, Reno, Nevada 89557

<sup>4</sup>University of California, Los Alamos National Laboratory, Los Alamos, New Mexico 87545

<sup>5</sup>Technische Universität Darmstadt, 64289 Darmstadt, Germany

<sup>6</sup>Max-Planck-Institut für Quantenoptik, 85748 Garching, Germany

<sup>7</sup>INRS-EMT, 1650 bd. L. Boulet, Varennes, Québec J3X 1S2, Canada

(Received 30 November 2006; accepted 5 March 2007; published online 17 May 2007)

The maximum energy of protons that are accelerated forward by high-intensity, short-pulse lasers from either the front or rear surfaces of thin metal foils is compared for a large range of laser intensities and pulse durations. In the regime of moderately long laser pulse durations (300–850 fs), and for high laser intensities  $[(1-6) \times 10^{19} \text{ W/cm}^2]$ , rear-surface acceleration is shown experimentally to produce higher energy particles with smaller divergence and a higher efficiency than front-surface acceleration. For similar laser pulse durations but for lower laser intensities ( $2 \times 10^{18} \text{ W cm}^{-2}$ ), the same conclusion is reached from direct proton radiography of the electric fields associated with proton acceleration from the rear surface. For shorter (30–100 fs) or longer (1–10 ps) laser pulses, the same predominance of rear-surface acceleration in producing the highest energy protons is suggested by simulations and by comparison of analytical models with measured values. For this purpose, we have revised our previous analytical model of rear-surface acceleration [J. Fuchs *et al.*, *Nat. Phys.* **2**, 48 (2006)] to adapt it to the very short pulse durations. Finally, it appears, for the explored parameters, that rear-surface acceleration is the dominant mechanism.

© 2007 American Institute of Physics. [DOI: 10.1063/1.2720373]

### I. INTRODUCTION

In the past few years, intense research has been conducted on the topic of laser-accelerated ion sources and their applications.<sup>1</sup> These ultrabright ion sources are accelerated from thin foils by irradiating them with ultraintense short laser pulses.<sup>2,3</sup> Thanks to the high beam quality<sup>4,5</sup> and short duration (at the source) of such novel, pulsed proton beams, in contrast to the ion beams produced before with longer, lower intensity lasers,<sup>6</sup> this research has opened new perspectives for important applications such as high-brightness ion sources,<sup>4</sup> radioisotope generation,<sup>7</sup> proton radiography of inertial fusion plasmas,<sup>8–10</sup> high-energy density matter and fusion studies,<sup>11</sup> or even medical use.<sup>12</sup>

There has been, however, a long-standing controversy regarding the origin of the accelerated protons: many experimental groups, using TW and PW short-pulse laser systems worldwide, have observed rather similar proton beam phenomena, but with conflicting interpretation. This matter of the origin of the ions, and of the acceleration mechanism, is of crucial importance in the prospect of properly optimizing the ion beam properties for any particular application. In the

range of target and laser parameters that will be studied here, there are two main mechanisms that lead to laser acceleration, in the forward direction, of high-energy protons from solids (we will not discuss here the mechanisms leading to ion acceleration in lower density plasmas<sup>13</sup>). First, at the laser-irradiated target surface, the laser pressure sets an electric field that pushes electrons inward, away from the interaction region. These electrons are originating from the preplasma existing at the target front surface, as is the case in all the experiments reported up to now with lasers having significant preleading energy ahead of the main pulse. We will not discuss here experiments performed at ultrahigh contrast<sup>14</sup> for which the ion acceleration mechanisms are however similar. The induced charge-separation field at the front interface accelerates the target surface forward. Ions initially at rest close to the surface can thus be accelerated to a maximum velocity that is twice the target surface recession speed. This results in front-surface acceleration (FSA) of ions into and through the target.<sup>15–18</sup> This process is observed to be predominant in producing the highest energy protons in some hybrid simulations, which, however, do not have a self-consistent evolution of the target resistivity.<sup>19</sup> Second, at the nonirradiated rear surface, fast electrons that have propagated through the target form a dense sheath that results in a strong electric field. The rear-surface acceleration (RSA)  $\sim TV/m$  electric field ionizes atoms and accelerates ions (that

<sup>a)</sup>Present address: Laboratoire pour l'Utilisation des Lasers Intenses, Palaiseau, France. Electronic mail: julien.fuchs@polytechnique.fr

<sup>b)</sup>Present address: CELIA, Université Bordeaux 1, CNRS, CEA, 33405 Talence, France.

expand together with the electrons in a quasineutral beam normal to the surface.<sup>13,20</sup> FSA produces a low-quality beam,<sup>21</sup> because of the stochastic nature of the laser-plasma interaction and hence of the charge separation field at the critical density interface. FSA has been clearly identified by nuclear activation<sup>22</sup> and neutron spectroscopy<sup>23</sup> techniques. Conversely, RSA can produce extremely laminar, low-emittance beams, and has been unambiguously demonstrated by accelerating ions (e.g.,  $F^{7+}$ ) from a thin source layer deposited on a substrate<sup>20,24</sup> and by suppressing energetic protons when perturbing the rear surface.<sup>25</sup> Since the accelerated protons stem from hydrogen-containing contaminants (e.g., water vapor) that are present on both the front and rear surfaces of the targets and since most experiments have used nonheated targets (heating can remove the contaminants layer), it is difficult to isolate the source of accelerated protons, which has led to the present controversy.

In addition to the FSA and RSA mechanisms, we should note that two additional processes have been observed in theoretical studies. The first one is the acceleration of ions by collisionless shocks.<sup>26</sup> For this process to be efficient, the shock must have a high Mach number, i.e.,  $M \geq 2$ . According to Ref. 26, ultrahigh laser intensities  $I \geq 3 \times 10^{22}$  W/cm<sup>2</sup> are therefore required for realistic solid density targets. In these conditions, simulations observe that shock-accelerated ions, although producing a beam of low quality,<sup>27</sup> can have similar or higher energies than rear-accelerated ones. The second process is a volumetric acceleration regime<sup>27,28</sup> in ultrathin targets where the laser pulse can propagate in the relativistic transparent regime.<sup>29</sup> Therefore, it also requires ultrahigh intensity (and ultrahigh contrast) laser pulses but could produce extremely high ion energies. These processes are, however, still waiting for experimental confirmation.

Numerical simulations have<sup>18,30–33</sup> observed, for laser intensities ranging from  $10^{17}$  to  $5 \times 10^{19}$  W/cm<sup>2</sup>, and for laser pulse durations from 10 to 500 fs, a predominance of RSA in producing the highest energy ions. Experimentally, a large number of results have been reported but few studies have been devoted to elucidate the acceleration mechanism. At low laser energy, it has been shown in spherical targets<sup>34</sup> that RSA was predominant but the respective angular distributions of FSA and RSA were not elucidated. At high laser energy ( $>1$  J), two experiments concluded that the highest energy protons originate from FSA.<sup>22,35</sup> In Ref. 35, this conclusion is reached using three target configurations: metal-only 100  $\mu$ m Al target, 100  $\mu$ m Al substrate coated with a thick 20  $\mu$ m hydrogeneous layer either at the front or at the rear of the substrate, with a minimization of the general hydrocarbon surface contamination by heating the target. The intensity is  $8 \times 10^{19}$  W/cm<sup>2</sup> and the pulse duration is of the order of 1 ps. The problem with this experiment is that it is difficult to compare directly the results of the various experimental configurations. In the case of a thick hydrogeneous layer associated with the Al substrate, the hot electron source (preplasma conditions at the front) is different depending on whether the layer is at the front or at the rear of the substrate. In addition, the hot electron transport in thick insulating layers is different from that in metal targets. It has been observed that filamentation of the laser-generated hot electrons

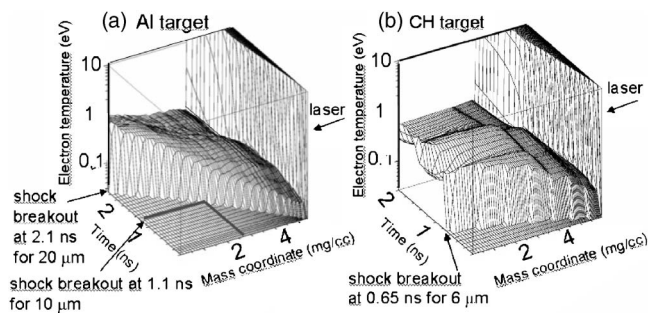


FIG. 1. 1D hydrodynamic simulations of preheating of a solid target by the ASE pedestal of a laser pulse using the MULTI code (Ref. 78). (a) In this case the target is composed of Al and the intensity of the ASE is  $6 \times 10^{12}$  W/cm<sup>2</sup>. (b) In this case the target is composed of CH and the intensity of the ASE is  $10^{13}$  W/cm<sup>2</sup> as in Ref. 22.

occurs as they propagate through the insulating layer,<sup>36</sup> producing in turn disruption of the proton beam topology and of the proton angular distribution.<sup>37</sup> Thus it is difficult to reach indisputable conclusions from experiments in which the electron source and the electron transport change from one target configuration to another. Regarding Ref. 22, we believe that the rear surface of the 6  $\mu$ m Mylar foil used in this experiment was preheated by the laser amplified spontaneous emission, i.e., ASE ( $\sim 10^{13}$  W/cm<sup>2</sup> at  $\lambda_0 = 1$   $\mu$ m). In such a case, a sharp gradient at the rear surface does not exist anymore and RSA cannot take place.<sup>9,25,38</sup> We have checked this experimentally. We have observed in our experiments that, with a lower ASE level of  $\leq 6 \times 10^{12}$  W/cm<sup>2</sup> of 1.5 ns duration, 20  $\mu$ m (and thicker) Al targets show an energetic collimated proton beam whereas with 10  $\mu$ m Al this beam disappears. These data and those of Ref. 22 are consistent with hydrodynamic simulations: shock wave preheating of the rear surface appears after 1.1 ns in a 10  $\mu$ m Al target, 2.1 ns in a 20  $\mu$ m Al target, and 0.65 ns in a 6  $\mu$ m CH target. This is illustrated in Fig. 1.

More recently, several experiments in well-controlled conditions have observed a strong predominance of RSA over FSA in accelerating the highest energy protons.<sup>38–41</sup> Using a sputtering technique to eliminate a known thickness of hydrocarbon and water vapor contaminants selectively from either the front or the rear surface of a thin (15  $\mu$ m Au) foil, it has been shown conclusively at high laser energy that RSA was producing more than 99% of high-energy protons<sup>40</sup> for a laser intensity of  $I \sim 10^{20}$  W/cm<sup>2</sup> and a laser pulse duration of  $\tau_L = 100$  fs. The highest energy protons were also observed to be produced by RSA in experiments ( $I \sim 10^{19}$  W/cm<sup>2</sup> and  $\tau_L = 150$  fs) where the ASE level ahead of the main pulse was varied systematically:<sup>38</sup> for a target thinner than an optimum determined by the ASE level, the proton maximum energy drops due to rear-surface preheating induced by ASE.

In this paper, after presenting the setup of the experiments (Sec. II) and of the particle-in-cell (PIC) simulations (Sec. III), we report on three sets of experiments where we observe a predominance of RSA in accelerating the highest energy protons. The first two sets of experiment use direct beam observation (Sec. IV A) and nuclear activation (Sec. IV B) induced by thin, cold deuterated-rich layers placed ei-

ther at the front or the rear surface of Al targets.<sup>41</sup> We deduce that under our laser conditions of high laser intensity [ $\sim(1-6)\times 10^{19}$  W cm<sup>-2</sup>] and relatively long pulse durations (300–850 fs), and for thin (20  $\mu$ m) metal foils, RSA produces a collimated ( $\leq 20^\circ$ ) beam of energetic protons  $>16$  MeV while FSA produces a high-divergence, low-energy ( $\leq 6$  MeV) beam. We find that for protons  $>3.5$  MeV, FSA accounts for  $<3\%$  of the total energy of the accelerated protons. The third set of experiments (Sec. IV C) is performed at the same laser pulse duration but lower laser intensity ( $\sim 2\times 10^{18}$  W cm<sup>-2</sup>) and still using thin targets. It uses complementary proton radiography to observe the spatial and temporal structure of the ion beam accelerated from the rear surface of a tilted thin metal foil. The velocity of the observed proton front matches the recorded energy of the highest energy protons. Finally, in order to unify all the available experimental results in a coherent picture, we compare, in Sec. V, measurements of published experiments to analytical estimates of FSA- and RSA-produced proton energy. We find that RSA predominates in producing the highest energy protons, even for high-intensity pulses [ $\sim(2\times 10^{18})-(6\times 10^{19})$  W cm<sup>-2</sup>] having very short pulse durations (30–60 fs).

## II. EXPERIMENTAL SETUP

The experiments were performed using the 100 TW laser at the Laboratoire pour l'Utilisation des Lasers Intenses (LULI), and the 30 TW Trident laser at the Los Alamos National Laboratory. Both are Nd:glass lasers that produce pulses of  $\sim 20$ – $30$  J of  $\lambda_0=1.057$   $\mu$ m light in the CPA<sup>42</sup> mode. The pulse duration and focal spot full width at half-maximum (FWHM) are 320 fs/6  $\mu$ m at LULI<sup>43</sup> and 850 fs/20  $\mu$ m at Trident, leading to peak intensities of  $6\times 10^{19}$  W/cm<sup>2</sup> at LULI and  $10^{19}$  W/cm<sup>2</sup> at Trident. Both systems have ASE  $\leq 6\times 10^{12}$  W cm<sup>-2</sup>, producing a preformed plasma with exponential scale lengths of  $\sim 30$   $\mu$ m up to  $\sim 10^{20}$  cm<sup>-3</sup> and  $\sim 3$   $\mu$ m up to solid density, as measured at LULI by a 0.3 ps interferometric probe at 0.35  $\mu$ m.<sup>44</sup> Unless stated otherwise, targets are irradiated at normal incidence.

## III. SETUP OF TWO-DIMENSIONAL PIC SIMULATION

In this work, the PIC simulations we perform to simulate the generation and transport of fast electrons, as well as the ion acceleration, are one- or two-dimensional (1D or 2D), collisional or collisionless. We have verified that, for the laser and target parameters that are covered in this paper, we can use collisionless PIC simulations to compare with our experiments since the mechanisms that can hamper the transport of fast electrons through the solid do not play an important role in our conditions. Transport of fast electrons through the solid can be modified by collective effects, via the self-induced magnetic fields, collisions, or by the lack of return current. Regarding the collective effects, in the multi-dimension simulations we have performed, either 2D or 3D, the intense magnetic fields only appear near the irradiation region and are reduced by orders of magnitude inside the target.<sup>45,46</sup> Therefore, in our experimental conditions, we be-

lieve that the magnetic fields are low inside the target and the anomalous stopping they induce does not have a strong effect in our conditions on MeV electrons, relevant to our case, that lead to ion acceleration. Regarding the effect of collisions, our previous work<sup>47</sup> and other simulations we have performed in this paper (see Sec. V) show that they do not influence significantly the transport of the MeV electrons. We have tested this in a situation in which the effect of the collisions could potentially be the highest, i.e., in a situation in which the incident laser intensity is low (around the threshold of relativistic intensities,  $10^{18}$  W cm<sup>-2</sup>; see Sec. V, which is devoted to a discussion of RSA and FSA at these low intensities) and for low, even zero, initial target electron temperature. In these simulations, we have observed no significant deviation in RSA fields between collisional and collisionless 1D PIC simulations. Furthermore, other works have also shown that collisionless PIC are relevant to simulate fast electron transport in dense conductors; see, e.g., Refs. 40, 48, and 49. Finally, regarding the effect of the target resistivity and of the return current, in the case in which the target resistivity is initially high, there is a transitory situation in which the fast electron flow could be reduced since the background electrons cannot provide current compensation. Our simulation starting with zero initial target electron temperature, however, shows that this transition from a room-temperature resistivity of the material used to the plasma state does not affect the bulk of the fast electrons transported to the rear surface and therefore other PIC simulations starting even at 1 keV initial electron temperature are valid in modeling the RSA fields. This meets the fact that, even in the case of insulator targets (CH), where the initial resistivity is the highest, we and others<sup>3</sup> have not observed experimentally a significant difference in the maximum energy of the collimated proton beam compared to using metal targets of the same thickness. The difference between these two situations lies mainly in the topology of the beam<sup>37</sup> which is filamented in the case of insulator targets, due to an instability of the ionization front associated with the first electrons propagating through the target.<sup>36</sup>

In the experiments, the laser is linearly polarized. To mock up the 3D configuration of the experiment in which the laser's linear polarization induces an anisotropy in hole boring and ion acceleration, we have performed the 2D simulations both with P and S polarization (pol.). Here P-pol means that the laser electric field is in the 2D simulation plane and the S-pol means that the electric field is perpendicular to the same plane. Then we have added the results of simulations made with P- and S-linear polarizations. It is interesting to note that since the P-pol laser is more absorbed than the S-pol one in the preformed plasma, it generates more energetic electrons and hence more energetic ions from the target rear side. However, the P-pol laser dissipates its energy into the preformed plasma quickly, and is less effective to accelerate the ions within the preformed plasma (i.e., the front-side ions). Inversely, the S-pol laser generates more energetic ions in the front side preplasma but at the same time generates less energetic electrons that can travel through the foil, so it is less effective in forming a sheath and accelerating ions from the rear surface.

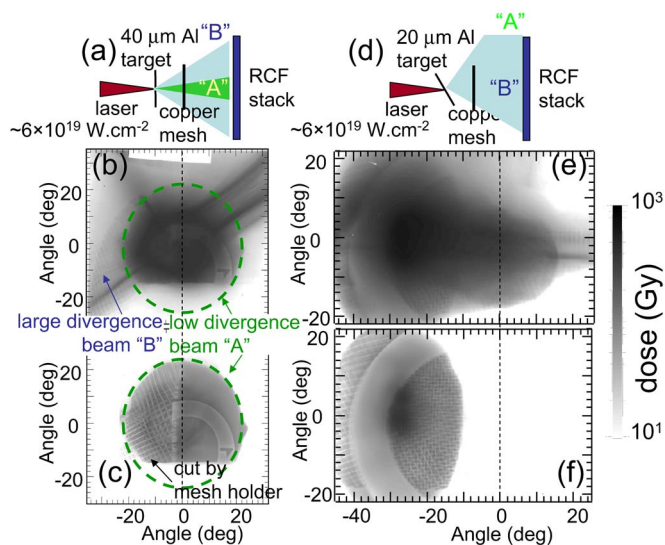


FIG. 2. (Color online) (a) Schematic of the experiment showing a double proton beam. For this shot, the RCFs sensitive layer is facing the proton beam. (b)  $\sim 2$  MeV and (c)  $\sim 4.5$  MeV RCF layers. (d)–(f) Same as (a)–(c) except that here the target is tilted by  $30^\circ$ . The observed structures in the proton beam are imprinted by the copper mesh.

In the simulations shown in Sec. IV A and IV B, the target substrate is a  $20 \mu\text{m}$  thick slab of  $40 \times n_c$   $\text{D}^+$  ions.<sup>50</sup> The simulation box is  $100 \mu\text{m}$  longitudinally and  $20 \mu\text{m}$  transversally. The target rear surface is covered by a water vapor layer ( $\text{H}^+(67\%)$ ,  $\text{O}^{6+}(33\%)$ ). The contaminant layer is estimated to be  $\sim 2$  nm thick.<sup>6</sup> To estimate the proportion of protons in the front-side preformed plasma (whose scale length is modeled from the interferometric measurements), we suppose that  $\text{H}^+$  and  $\text{D}^+$  are homogeneously mixed up to  $n_c$ . Such plasma corresponds to an ablated 2 nm of water vapor plus an additional ablated 62 nm of  $\text{D}^+$ . This implies a proton proportion in the plasma of  $\sim 3\%$ . Note that this maximizes the estimated concentration of  $\text{H}^+$ : if those were fully mixed with  $\text{D}^+$  up to solid density (or if the  $\text{H}^+$  would run in the front of the preformed plasma), the  $\text{H}^+$  proportion could be as low as 0.03%. In the simulations we did not

include the first, longer density gradient observed in the experiments since test 2D-PIC simulations of laser propagation for  $100 \mu\text{m}$  up to a density  $0.1n_c$  (the observed inflection point between the two plasma scale-lengths) either with only the shorter ( $3 \mu\text{m}$ ) or the two ( $30 \mu\text{m}$  and  $3 \mu\text{m}$ ) scale-length preplasmas did not exhibit any significant difference in laser propagation or in characteristics of ion acceleration. The simulation was run up to 1 ps, at which time acceleration of the high-energy ions ends. Lower-energy ions will be produced over longer times as well as from wings of the laser pulse that are not accounted for in the simulations. This does not, however, affect our conclusions since we concentrate on the high-energy part (2 MeV) of the ion spectra.

## IV. RESULTS

### A. Direct beam observations

As shown in Fig. 2, two proton beams with distinct angular and energy distributions are observed to be accelerated from untreated thin ( $20$  and  $40 \mu\text{m}$ ) Al solid targets irradiated at  $6 \times 10^{19} \text{ W/cm}^2$  by the 320 fs laser pulse. The protons are detected in multiple layers of radiochromic film (RCF) densitometry media.<sup>51</sup> The RCFs used here are asymmetric,<sup>52</sup> with their sensitive layer facing the incident proton beam. The spatial distribution of the protons in a given RCF layer gives the angular emission pattern at a known interval of proton energy.<sup>3,9</sup> The first beam (“A”), collimated to a half-angle of  $\sim 20^\circ$ , penetrates in successive RCFs (only the first two are shown). The second beam (“B”), having a larger divergence than the first ( $>50^\circ$ ), appears only in the first RCF. Only beam “A” was observed when the RCFs in the stack were swapped so that the sensitive layer was not facing the incident proton beam, i.e., more Mylar has to be crossed before reaching the sensitive layer [see Fig. 3(a)]. This is shown in Figs. 3(b) and 3(c). In this case, beam “B” is of such low energy that it does not impress even the first RCF. This implies that the widely spread beam “B” has a maximum energy (above the RCF detection threshold)  $< 3$  MeV. When the target was tilted, as shown in Figs.

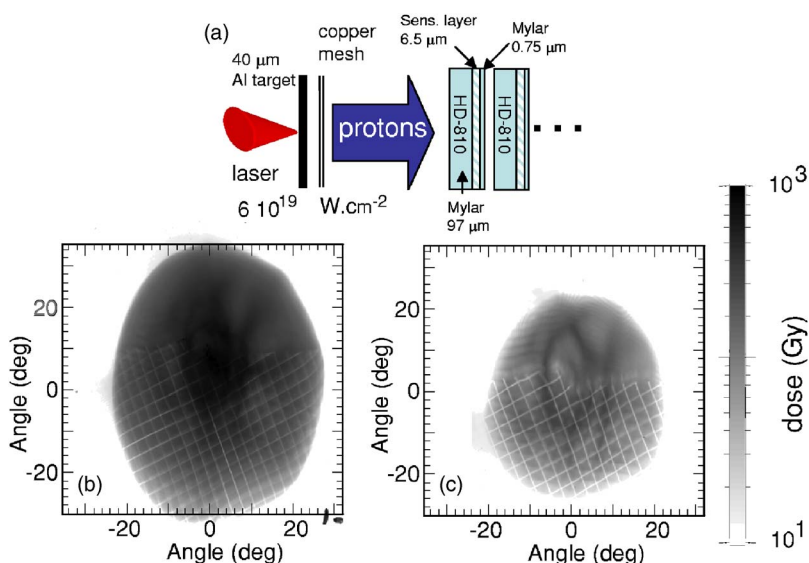


FIG. 3. (Color online) same experiment as in Fig. 2 except that, as illustrated in (a), the asymmetric RCFs are swapped so that the sensitive layer is not facing the proton beam. (b)  $\sim 3$  MeV and (c)  $\sim 4.5$  MeV RCF layers. The observed structures in the proton beam are imprinted by the copper mesh.

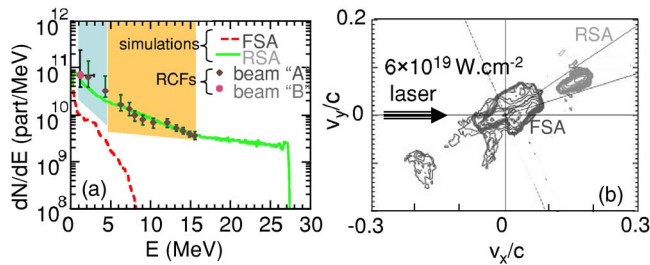


FIG. 4. (Color online) (a) Simulated angularly integrated  $H^+$  spectra overlaid with the experimental spectrum (limited by the number of used RCF layers). The RCF sensitivities used are indicated in color. The RSA spectrum low-energy cutoff is due to  $H^+$  contaminant depletion in the simulation. (b) Simulated phase-space distribution of the FSA and RSA  $H^+$  at  $t=400$  fs after the peak of the P-pol laser interaction. The target is tilted by  $25^\circ$ . Each contour line corresponds to every  $10^{0.3}$  of the ion number in a log scale.

2(d)–2(f), we observed that the centroid of beam “A” followed the target normal. Regarding beam “B,” since it has a large divergence, it is more difficult to track its centroid.

2D PIC simulations performed in the conditions of the experiment shown in Figs. 2(d)–2(f) suggest that beam “A” (high energy, low divergence) is produced by RSA while beam “B” (low energy, large divergence) results from FSA. Similar observations of FSA and RSA beams were previously made using 3D PIC simulations.<sup>31</sup>

The FSA beam of Fig. 4, consistent with the observed beam “B” of Fig. 2, has a rapidly decreasing energy spectrum and a large divergence. FSA is expected to produce a large-divergence beam because the critical density ( $n_c$ ) interface where the charge separation occurs is curved by the hole boring of the laser into the preplasma. The beam is centered along the target normal since the charge separation interface is compressed inwards by the laser and thus tends to be tilted, following the target surface.<sup>53</sup> The RSA beam, consistent with beam “A” of Fig. 2, is well collimated, and clearly normal to the target rear surface with a slowly decreasing spectrum. Noticeably, the high-energy portion of the proton spectrum [Fig. 4(a)] shows a large predominance of RSA over FSA. We checked that, in the simulations, the FSA energy spectrum does not change significantly with a proton ratio below 10% since FSA is dominated by the abundant species ( $D^+$ ), thus the proton acceleration is less effective than for a pure proton plasma.

## B. Nuclear activation measurements

To confirm the prediction of the PIC simulations and the predominance of RSA over FSA for high-energy protons, we compare the simulations to measured deuterons accelerated selectively from a  $0.5 \mu\text{m}$  thick  $\text{CD}_2$  layer that we deposited *only* on one side of an Al foil. As in Ref. 22, the accelerated  $D^+$  were discriminated from other ions by use of the  $^{10}\text{B}(d,n)^{11}\text{C}$  nuclear reaction in a very high purity (99.82%)  $^{10}\text{B}$  catcher foil [see Fig. 5(a)]. The boron activation “catchers” were 1 cm diameter by 3 mm thick, and placed 4.5 mm behind the target foil to stop deuterons or protons emitted within a half-angle of  $48^\circ$  with respect to the laser focus. We also used, in an alternate shot, a  $^{11}\text{B}$  catcher in order to measure protons through the  $^{11}\text{B}(p,n)^{11}\text{C}$  nuclear reaction.

After each shot, the catcher was placed between two NaI scintillation detectors to measure the  $^{11}\text{C}$  beta-decay time series by the coincident detection of the 511 keV positron-annihilation quanta. The total  $^{11}\text{C}$  yield was determined from the integral of the 20.38 min half-life decay curve (see Fig. 6), accounting for the shot time and the 30% detection efficiency (calibrated with  $^{22}\text{Na}$  sources). For similar laser energy, we observed very similar  $^{11}\text{C}$  yields in the two experiments, i.e., using the LULI and Trident lasers.

In past experiments, we used small aperture magnetic spectrometers to measure ion energy spectra, and, as here, multilayer radiochromic film and CR-39 stacks to measure the spatial distribution of protons up to angles of  $20^\circ$  from the laser direction. As PIC simulations indicate that the angular divergence of FSA ions is larger than this, and that their spatial distribution may be nonuniform, the catcher-activation technique appears well adapted to the situation. It allows integrating all the accelerated ions over a large angular acceptance, and is immune to saturation effects.

Figure 5(c) presents, for a laser intensity of  $10^{19} \text{ W cm}^{-2}$  and a pulse duration of 850 fs, the measured  $^{11}\text{C}$  yield for FSA  $D^+$  and for different thicknesses of the Al substrate. For target thicknesses of 20–100  $\mu\text{m}$ , we measure a rapid reduction of the  $^{11}\text{C}$  activation yield, consistent with a slowing down of the FSA  $D^+$  due to their passage through the substrate foil. Note that the front-accelerated ions that are measured this way are not influenced by the rear-side intense sheath field when they reach the rear surface. Indeed, in the 2D PIC simulation, the front accelerated ions maximum velocities are about a tenth of the light velocity. The traveling time through the 20  $\mu\text{m}$  target is then  $\sim 700$  fs, which is about the pulse length for this experiment. Therefore, the sheath field at the rear side is negligible when the front-accelerated ions cross the rear surface, because the field quickly drops (the peak field drops with a characteristic exponential decay time of  $\sim 700$  fs<sup>64</sup>) after the pulse is turned off.

For RSA  $D^+$ , we measure a  $9 \times 10^5$   $^{11}\text{C}$  yield for a 20  $\mu\text{m}$  target. Compared to Ref. 22, RSA  $D^+$  acceleration is possible because we use thicker targets. The  $^{11}\text{C}$  yield decreases with target thickness as the RSA field is reduced due to the increased spread of the hot electrons in the target. Indeed, as the RSA field is decreased, there is less  $D^+$  accelerated by RSA with less energy and this decreases the  $^{11}\text{C}$  yield, as observed. Note that the protons are preferentially accelerated by RSA due to their smaller mass. This is clearly seen in the longitudinal phase plot of ions, Fig. 5(e). The deuterons, sensing a reduced sheath field, are therefore accelerated to lower energies than the protons. Note that the  $D^+$  maximum energy is lower as compared to the case in which there is no proton on the target surface. In this case, more energetic deuterons are coming from the rear side of the target.

In order to relate the incident ion fluence on the catcher to the measured  $^{11}\text{C}$  yield, we model the nuclear activation measurements by means of a Monte Carlo (MC) code. This code determines the angle-integrated  $^{11}\text{C}$  yield in either a  $^{10}\text{B}$  or  $^{11}\text{B}$  catcher. It uses given  $D^+$  and  $H^+$  angularly resolved

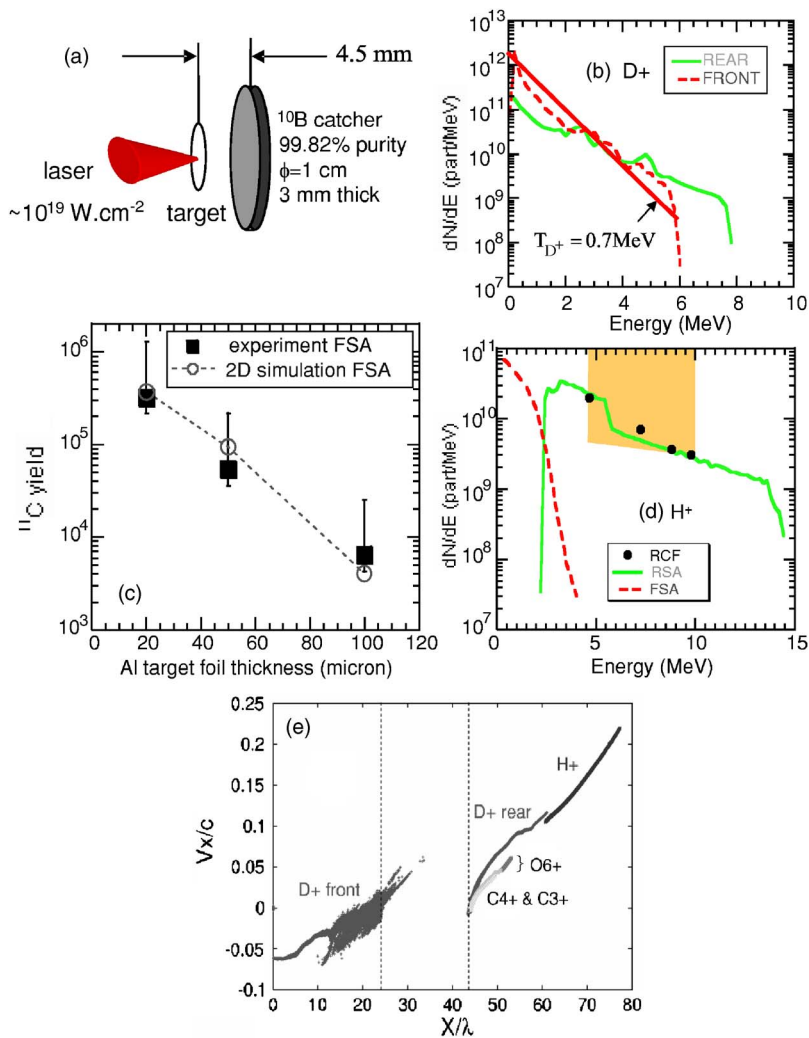


FIG. 5. (Color online) (a) Setup of the activation experiment at  $10^{19} \text{ W cm}^{-2}$ . (b) Simulated  $\text{D}^+$  spectra for a  $20 \mu\text{m}$  foil. The RSA  $\text{D}^+$  have lower energy than if the  $\text{H}^+$  layer would be absent since, due to their smaller mass, the  $\text{H}^+$  are preferentially accelerated by RSA. (c) Experimental and simulated  $^{11}\text{C}$  yield for FSA  $\text{D}^+$ . (d) Simulated  $\text{H}^+$  spectra overlaid with the RCF inferred spectrum, both for a  $20 \mu\text{m}$  foil. All spectra are angularly integrated. (e) The phase plots  $X-V_x$  of ions at 1 ps. The broken lines indicate the initial Al target surface.

spectra and calculates in 3D the propagation of the particles through the foil and catcher (only for the ions generated in the  $\pm 48^\circ$  acceptance of the catcher). It takes into account energy loss and angular scattering, both in the target and the

catcher, using the code SRIM,<sup>54</sup> and calculates the  $(d,n)$  or  $(p,n)$  reaction rate using their known cross sections.<sup>55</sup>

A first approach to determine the spectrum of the FSA  $\text{D}^+$  that matches the data of Fig. 5(c) is to use a Maxwellian spectrum with a high-energy cutoff.<sup>56</sup> The value of the cutoff proves to be very sensitive to fit the slope of the  $^{11}\text{C}$  yield as a function of the Al substrate thickness. The best fit is obtained for  $T_{\text{D}^+} = 0.7 \text{ MeV}$  and a cutoff of 6.1 MeV. This cutoff value is higher than deduced from neutron spectroscopy measurements in other experiments,<sup>53,57</sup> however these experiments have been performed with lower preplasma scale length, which reduces the hot electron temperature<sup>58</sup> and hence the FSA ion energy. As shown in Fig. 5(b), the values we deduce for the cutoff and the temperature are in very good agreement with the FSA  $\text{D}^+$  spectrum obtained from PIC simulations performed at  $10^{19} \text{ W cm}^{-2}$ , i.e., in the conditions of the experiment.<sup>59</sup> The PIC simulation spectrum at  $10^{19} \text{ W cm}^{-2}$  also fits very well the experimental  $^{11}\text{C}$  yield as a function of the substrate thickness, as shown in Fig. 5(c). Note that for similar PIC+MC simulations performed at different laser intensities, there is a significant deviation (by orders of magnitude) in the simulated slope as compared to the experimental one. Using the simulated RSA  $\text{D}^+$  spectrum, we also get a good agreement between the experimental (9

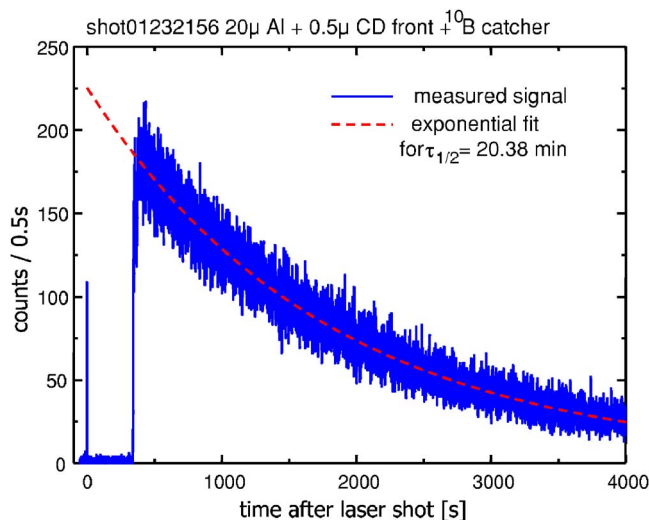


FIG. 6. (Color online) FSA  $\text{D}^+$  activation data for a shot on a  $20 \mu\text{m}$  thick Al. The target front surface is covered with a  $0.5 \mu\text{m}$  thick layer of  $\text{CD}_2$ .

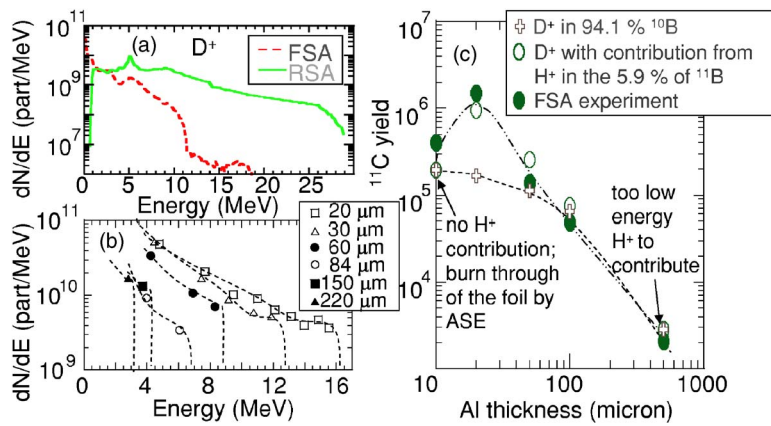


FIG. 7. (Color online) Activation experiment at  $6 \times 10^{19} \text{ W cm}^{-2}$ . (a) Simulated  $\text{D}^+$  spectra for a  $20 \mu\text{m}$  foil, (b) RCF inferred experimental  $\text{H}^+$  spectra for different Al foil thicknesses (the lines are guides for the eye), (c)  $^{11}\text{C}$  yield for FSA  $\text{D}^+$ , experimental (filled circles) and simulated with (empty circles) or without (diamonds) the contribution from  $\text{H}^+$  in  $^{11}\text{B}$  inferred from the spectra shown in (b). All spectra are angularly integrated.

$\times 10^5$ ) and simulated ( $8.5 \times 10^5$ )  $^{11}\text{C}$  yield for the RSA  $\text{D}^+$  for a  $20 \mu\text{m}$  target. Using the simulated proton spectrum, we also obtain a good agreement between the experimental ( $8 \times 10^5$ ) and simulated ( $2 \times 10^6$ ) proton-induced  $^{11}\text{C}$  yield in a  $^{11}\text{B}$  catcher for both front- and rear-surface protons in the case of a  $20 \mu\text{m}$  target.

The measured FSA  $\text{D}^+$  peak energy is an upper boundary of the FSA proton peak energy. In fact, the FSA proton cutoff is expected to be  $\sim 1/2$  of the  $\text{D}^+$  one, i.e.,  $\sim 3 \text{ MeV}$ , since FSA  $\text{D}^+$  and  $\text{H}^+$  have the same velocity (see below Sec. V), consistent with Figs. 5(b) and 5(d). As the RCF show collimated high-energy protons, at least up to  $10 \text{ MeV}$  [see Fig. 5(d)], these can be only RSA protons, in agreement with the PIC simulation. This confirms the predominance of RSA over FSA at high ion energy. Quantitatively, we can assess that for a  $20 \mu\text{m}$  thick target, the RSA proton beam contains  $53 \text{ mJ}$  above  $3.5 \text{ MeV}$  ( $56 \text{ mJ}$  over all the spectrum, i.e.,  $0.3\%$  of the laser energy). Conversely,  $25 \mu\text{J}$  are, at most, contained in the front proton beam over the same range ( $12 \text{ mJ}$  over the entire spectrum). Indeed, the energy in the FSA protons could be in reality much smaller since we deliberately maximized the proportion of protons in the front-side preformed plasma.

Similar results are obtained when performing the experiment at higher intensity, namely  $6 \times 10^{19} \text{ W cm}^{-2}$  (see Fig. 7). In this case, the activation target was an isotopically enriched boron catcher ( $94.1\% \text{ }^{10}\text{B}$ ,  $5.9\% \text{ }^{11}\text{B}$ ). The small admixture of  $^{11}\text{B}$  caused some poisoning of the  $^{11}\text{C}$  yield by the protons due to  $^{11}\text{B}(p,n)^{11}\text{C}$  activation. The level of poisoning was experimentally assessed by measuring the protons spectra for various Al target thicknesses, as shown in Fig. 7(b). Note that we only need to assess the total proton spectrum for energies above  $3 \text{ MeV}$  since this is the reaction threshold for the  $^{11}\text{B}(p,n)^{11}\text{C}$  reaction.<sup>60</sup> When taking in account the contribution of the proton and the simulated  $\text{D}^+$  spectra [see Fig. 7(a)], we obtain a good agreement between the simulated and experimental  $^{11}\text{C}$  yield for FSA  $\text{D}^+$ , as shown in Fig. 7(c). The total PIC-simulated proton spectrum compares well with that inferred from RCF, as shown in Fig. 4(a). At this intensity, we can assess that for a  $20 \mu\text{m}$  thick target, the RSA proton beam carries  $175 \text{ mJ}$  in the experimentally observed  $3.5\text{--}16 \text{ MeV}$  range ( $275 \text{ mJ}$  over all the simulated spectrum, i.e.,  $\sim 1\%$  of the laser energy). Conversely,  $4 \text{ mJ}$  are, at most, contained in the FSA proton beam

over the same range ( $9 \text{ mJ}$  over the entire spectrum). For thicker targets, both mechanisms will produce lower energy protons because the RSA field is reduced<sup>38,61</sup> and because FSA protons are slowed down in the target. For thickness  $\leq 60 \mu\text{m}$ , since FSA protons are  $\leq 7 \text{ MeV}$ , RSA is still predominant, as attested by Fig. 7(b), which shows that higher proton energies are observed. For target thickness  $\geq 85 \mu\text{m}$ , the proton energies observed in Fig. 7(b) become consistent with FSA protons slowed down in the target, hinting that FSA could become then predominant.

In summary, using direct beam observation and nuclear activation measurements, we have shown that RSA predominates over FSA in producing the highest energy protons from thin foils and for high laser intensities [ $(1\text{--}6) \times 10^{19} \text{ W/cm}^2$ ] of short duration ( $320\text{--}850 \text{ fs}$ ). For thicker foils, RSA fields are reduced due to hot electron spread within the foil and FSA could become predominant.

### C. Proton radiograph of the electric fields associated with proton acceleration

Complementary to the previous measurements, but in a lower range of laser intensity, we have measured directly, using proton radiography, the electric fields that are on the rear surface of a laser-irradiated  $10 \mu\text{m}$  thick Au foil. The longitudinal extension of this electric field structure is seen to develop (i) in time at a speed that matches well the observed maximum energy of the protons accelerated from the radiographed target, and (ii) perpendicular to the tilted target surface, consistent with previous observations of rear-surface accelerated ions.<sup>3</sup> This measurement extends to a lower laser intensity the results obtained in the previous section in the sense that the most energetic protons correspond to an acceleration that takes place on the target rear surface.

This direct measurement is achieved using proton deflectometry of an auxiliary transverse proton beam.<sup>62</sup> For this experiment, we used two intense short pulses produced by the  $100 \text{ TW}$  LULI laser facility. Two laser pulses of  $\sim 15\text{--}20 \text{ J}$  of  $1 \mu\text{m}$  light were compressed independently, one (“beam 1”) to  $320 \text{ fs}$  and the other (“beam 2”) to  $1.5 \text{ ps}$ . As illustrated in Fig. 8(a), the two laser beams were focused, at close to  $90^\circ$  from each other [see Fig. 8(a)], down to  $\sim 6 \mu\text{m}$  ( $11 \mu\text{m}$ ) FWHM for beam 1 (beam 2). This led to peak intensities on target of  $\sim 6 \times 10^{19}$  ( $2 \times 10^{18}$ )  $\text{W cm}^{-2}$  for

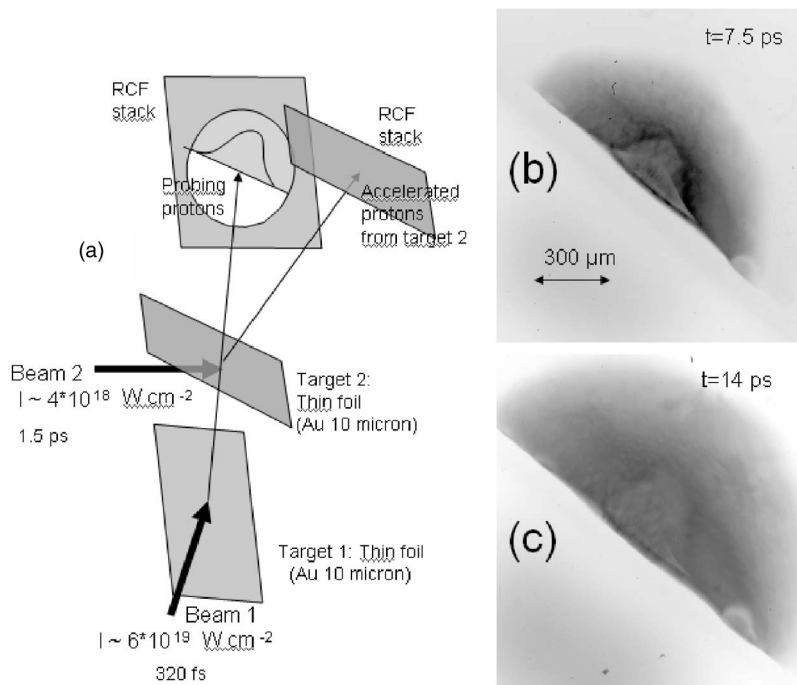


FIG. 8. (a) Experimental setup of the proton radiograph. Target 2 is tilted at  $45^\circ$  with respect to the axis of beam 2. The distance between the focus points of beam 1 and beam 2 is 2 mm. (b) and (c) Probing proton angular distributions (for the same shot) at 3.15 cm from target 1 for the proton probe beam shown in (a) and for different times of arrival on the edge of target 2 (as indicated on each film). Magnification is 15.75. Time 0 refers to the irradiation of target 2 by beam 2.

beam 1 (beam 2). The two proton beams generated by the irradiation of the two beams on solid targets were detected in multiple layers of RCF.

Beam 1 was delayed with respect to beam 2 so that the proton probe beam could probe the proton accelerating phase on the rear surface of target 2. As the proton probe beam has a broad energy range, protons of different energies cross the expanding plasma from the rear side of target 2 at different times. As these different proton energies correspond to different layers of RCF, it allows us to obtain a temporal evolution<sup>62</sup> of the plasma expansion through the deflections that the fields associated with the expansion induce on the probing protons.

We have to consider that the electrostatic field  $E_\perp$  applies not only on the probing protons but also on the comoving electrons that accompany them (see Fig. 9). As the probing plasma beam has expanded and diverged from target 1 when it interacts with the plasma flowing from target 2, we can estimate that for the case of Figs. 8(b) and 8(c), the probing beam density is reduced to  $n \sim 3 \times 10^{14} \text{ cm}^{-3}$ , leading to a local Debye length of  $\sim 400 \mu\text{m}$ . This means that the plasma is unable to shield the electrostatic field at the ion front when passing through it since the field extension is much smaller than the Debye length. Now, the protons and electrons will experience opposite deflections due to the field, the deflection being much smaller for the protons. This will induce a charge-separation field  $E_c = en\delta x S / \epsilon_0$ , where  $S \sim 700 \mu\text{m}$  is the typical lateral dimension of the probing beam when crossing the field. The deflection  $\delta x$  induced by the field on the electrons can be estimated knowing the transverse momentum given to the electron by the probed electric field. This momentum is  $m_e v_\perp = e E_\perp \tau$ , where  $\tau$  is the crossing time in the field, i.e.,  $\tau \sim \Phi / v_\parallel$ , where  $\Phi$  is the transverse dimension of the field structure expanding from target 2, estimated from the film of Figs. 8(b) and 8(c) as  $\sim 60 \mu\text{m}$ ,

and  $v_\parallel$  is the probing proton longitudinal velocity. The angular deflection of the probing electrons is  $\theta \sim v_\perp / v_\parallel = e E_\perp \Phi / (m_e v_\parallel^2)$ . Thus  $\delta x = \theta \Phi \sim 400 \mu\text{m}$ , yielding  $E_c \sim 5 \times 10^5 \text{ V/m}$ . Note that this field will be shielded anyway by the plasma flowing from target 2 that has a Debye length of  $\sim 100 \mu\text{m}$ . As the magnitude of  $E_c$  is much smaller than the external field  $E_\perp$ , its effect will be negligible and we can consider that the deflected electrons will be lost in the probed plasma (the deflection brings them to target 2) and that the protons will propagate with the given impulse up to the RCF, unperturbed by the charge separation. We have also checked that the Coulomb (space-charge) force acting on the non-

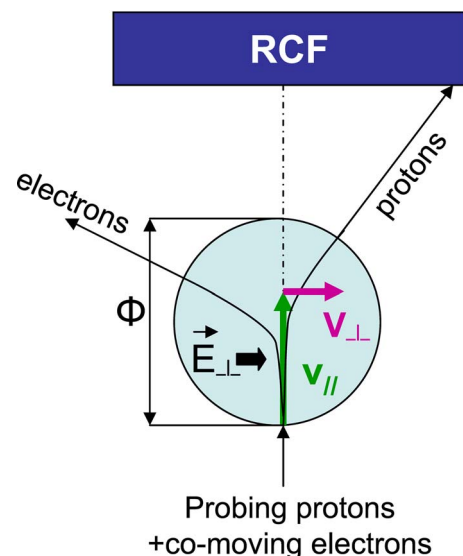


FIG. 9. (Color online) Schematic of the deflection incurred by the probing protons and the comoving electron in the field structure induced by the plasma expansion from target 2 (see Fig. 8).

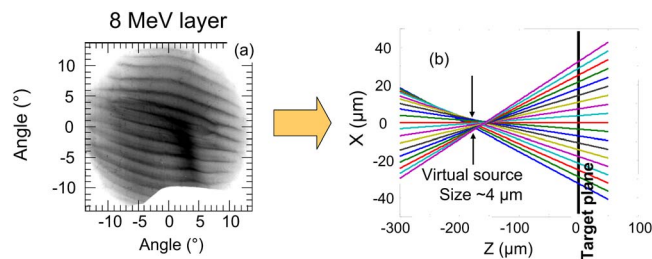


FIG. 10. (Color online) (a) Angular distribution of protons centered around 8 MeV accelerated from a  $60\ \mu\text{m}$  thick Al flat target irradiated at  $4 \times 10^{19}\ \text{W}/\text{cm}^2$  and detected on the RCF film stack placed 71 mm from the target. Beam fiducials induced by a 1D modulation (with a modulation period of  $3.6\ \mu\text{m}$  and a depth of 200 nm) on the target rear surface map the emission zone at the source (Refs. 4 and 63). This gives, therefore, access, for each fiducial beamlet, to its emission position on the target surface and to its emission angle. (b) Reconstruction of each beamlet trajectory in a plane perpendicular to the target surface. The ion flow is from left to right. The target plane is indicated. Each beamlet can be prolonged backwards (i.e., toward the incident laser) to reconstruct the virtual proton source. The envelope of the reconstructed beamlets defines a minimum source size of  $4\ \mu\text{m}$  diameter.

neutral protons does not induce a significant expansion of the beam that could perturb the deflection given by the probed electrostatic field.

As we use here a point projection technique, the spatial resolution of the measurement is determined by the source size of the probing protons. For our conditions, the physical source on target 1 is  $\sim 60\text{--}100\ \mu\text{m}$ , as can be seen in Fig. 10(a), but as the source is extremely laminar, it is equivalent to a virtual source.<sup>5</sup> As can be seen in Fig. 10(b), this virtual source is positioned  $\sim 150\ \mu\text{m}$  behind the target within a radius  $\sim 2\ \mu\text{m}$ , which determines the achievable resolution. The temporal resolution depends on the energy resolution of each RCF and the intrinsic source duration that is of the order of a few ps at most.<sup>63</sup> Typically, for the RCF used, the resolution is of the order of 1 ps.

The electric fields in the sample region are revealed by the proton deflection and the associated modifications in the proton density pattern. As expansion of the plasma takes place into vacuum, the electrons cool down and the decreasing electrostatic field is localized at the moving ion front.<sup>64</sup> This induces a local accumulation of moderately deflected protons near the expanding ion front, leading to the observed bell-shaped increase of probing proton dose in Figs. 8(b) and 8(c).

The speed of expansion inferred from the front of the proton deflection, i.e., the ion expansion front, is  $\sim 2.5 \times 10^7\ \text{m/s}$ . This speed is consistent with the observed  $\sim 4\ \text{MeV}$  maximum energy for the protons accelerated from target 2. At this intensity, lower than used for the experiments of Sec. IV A and IV B, we therefore also observe that the highest energy protons are accelerated from the target rear surface.

## V. GENERAL DISCUSSION REGARDING RSA VERSUS FSA

The aim of this section is to give a broad picture of RSA versus FSA, still in the perspective of the acceleration of the

highest energy protons. We have seen in the previous section that, in our experiment at high laser intensities [ $(2 \times 10^{18})\text{--}(6 \times 10^{19})\ \text{W}/\text{cm}^2$ ] and relatively long laser pulse durations (300–850 fs), RSA is predominant in accelerating the highest energy protons.

As mentioned in Sec. I, PIC simulations<sup>18</sup> have observed the same phenomenon of RSA predominance for laser intensities ranging from  $10^{17}$  to  $5 \times 10^{19}\ \text{W}/\text{cm}^2$ , and for laser pulse durations from 10 to 500 fs, although, as the simulations are 1D, the final proton energies are overestimated for both mechanisms. We have mentioned in Sec. III that we had previously tested that collisional stopping was not important enough to hamper the transport of MeV electrons and the efficiency of RSA. We have extended this test for low laser intensity and initial electron temperature range, since it is in these conditions that the collisional stopping would be stronger, by performing a complementary 1D PIC simulation of the interaction of a 53 fs laser pulse duration at an intensity of  $5.5 \times 10^{18}\ \text{W}/\text{cm}^2$  with a  $20\ \mu\text{m}$  thick target with the collisional PIC code PICLS. PICLS was operated with fourth-order interpolation for current and field calculation to avoid numerical heating completely. We started the simulation with zero initial electron temperature, and we did not observe any unphysical energy violation due to numerical problems. The binary collision module of our code is based on Takizuka and Abe's model,<sup>65</sup> extended to treat correctly relativistic collisions<sup>66</sup> and collisions between weighted macroparticles.<sup>67</sup> The Coulomb logarithm is calculated in-line with the ratio of projectile electron wavelength to Debye length.<sup>65</sup> Our collision model is the Spitzer description, which is proportional to  $1/T_e^{3/2}$ , since then the frequency will be infinite at the extremely low temperature in a degenerated plasma. The degeneracy temperature is about 6 eV at solid density,<sup>67</sup> which is sufficiently low and justifies our Spitzer model in simulations. In the test simulation, the hot electron temperature is  $\sim 315\ \text{keV}$ . The collisional mean free path of these electrons is about 0.05 cm in the Al target, which is much longer than the target thickness. As shown in Fig. 11, this simulation displays a large predominance of RSA in producing the highest energy protons. The maximum proton energy is the same as the collisionless case with the same simulation parameter. As a consequence, the collisional stopping cannot suppress the RSA, and it therefore confirms that the predictions of the previous collisionless simulations of Ref. 18 in the same range of parameters are indeed valid.

Regarding experimental evidence, published data at short pulse durations show that the recorded proton beam characteristics are consistent with the RSA beam observed here: acceleration normal to the target rear surface with a well-defined beam envelope having a maximum half-angle of  $\sim 10\text{--}20^\circ$ .<sup>68,69</sup> We have also performed experiments with pulses up to 10 ps duration<sup>61</sup> and observed the same beam characteristics, suggesting the predominance of RSA for all these various pulse durations.

However, most of the experiments simply report on the observed maximum energy of the accelerated protons. These can be compared to analytical estimates of the maximum proton energies  $E_{\text{max/front}}$  and  $E_{\text{max/rear}}$  coming, respectively, from the front and rear surfaces. At the laser-irradiated target

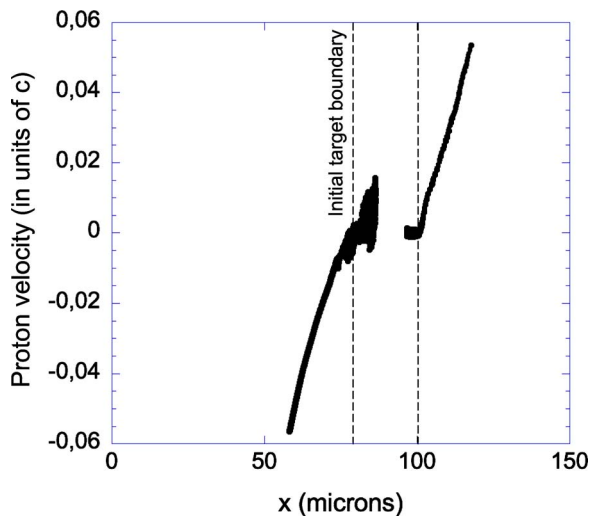


FIG. 11. Proton phase space obtained with a 1D PIC simulation of a  $5.5 \times 10^{18}$  W/cm<sup>2</sup>, 53 fs, for a 20  $\mu$ m target at 40  $n_c$ . The center of the target is composed of aluminum with proton layers on each side of 4  $\mu$ m thickness. There is an exponential preplasma on the target front surface extending from  $10^{-3} n_c$  to 40  $n_c$  in 5  $\mu$ m. The simulation box is 200  $\mu$ m long. The mesh size is  $\Delta x = 10$  nm and there are 260 particles per species per cell. The time step is equal to  $3.3 \times 10^{-2}$  fs. The temporal profile is Gaussian and the pulse is injected at the left-hand side of the simulation box. It interacts with the target at normal incidence, and its electric field is  $p$ -polarized. The snapshot is obtained at 1.6 ps after the time of the peak of the pulse has irradiated the front surface of the target.

front surface, the maximum velocity of the accelerated protons is given by twice the recession speed of the plasma surface.<sup>15,31</sup> In the case of total back reflection of the laser beam (i.e., when the efficiency of the laser piston is maximum), this recession speed is expressed as<sup>17</sup>

$$\frac{u_S}{c} = \sqrt{\frac{1 n_e Z m_e}{2 n_e M_i} a_0^2},$$

where  $n_e$  is the electron density at the reflection point, i.e.,  $n_e = \gamma n_c$ ,<sup>70</sup> where  $\gamma$  is the Lorentz factor of an oscillating electron in the laser field, i.e.,  $\gamma = (1 + a_0^2)^{1/2}$ , with  $a_0^2 = (p_{\text{osc}}/mc)^2 = I \lambda_\mu^2 / (1.37 \times 10^{18})$ , where  $I$  is the laser intensity in W cm<sup>-2</sup> and  $\lambda_\mu$  is the laser wavelength in micrometers. Therefore,  $E_{\text{max/front}} = 2 \cdot M_i \cdot u_S^2 = Z m_e c^2 a_0^2 / \gamma$ . Note that this estimate is consistent with measured values for FSA protons.<sup>23,38</sup>

This has to be compared with the maximum energy that can be gained by protons accelerated at the rear. A simple estimate of the maximum energy that can be gained by the accelerated ions based on a self-similar fluid theory<sup>56</sup> is

$$E_{\text{max/rear}} \sim 2Z\phi_{\text{ponderomotive}} \cdot \{\ln[t_p + (t_p^2 + 1)^{1/2}]\}^2,$$

where  $t_p = \omega_{pi} \cdot t_{\text{acc}} / (2^* \exp[1])^{1/2}$  with  $t_{\text{acc}}$  the acceleration time and  $\omega_{pi} = \sqrt{n_{e0} Z e^2 / m_i \epsilon_0}$  the ion plasma frequency ( $n_{e0}$  is the initial electron sheath density and  $m_i$  is the ion mass). In this approach, we compensate the fact that we maintain a constant temperature for the hot electron population driving the ion acceleration by a finite acceleration time. In reality, there is no limit in time for the acceleration but the expansion is adiabatic, the hot electron temperature decreasing progressively as the energy is transferred to the ions. This

approach was in good agreement with experimental results for laser intensities ranging from  $2 \times 10^{18}$  to  $6 \times 10^{19}$  W cm<sup>-2</sup>, and for laser pulse durations from 150 fs to 10 ps.<sup>61</sup> Refining this approach, we have found that for very short pulse durations, the acceleration time is no longer proportional to the laser pulse duration but tends toward a constant value. Indeed, even for very short pulses, there is a minimal time for the energy transfer from the electrons to the ions that needs to be taken into account. Also, for low laser intensities, this acceleration time has to be increased since the expansion is slower. These improvements to the RSA analytical model will be presented in detail in a separate publication.<sup>71</sup> Here we use  $t_{\text{acc}} = \alpha \cdot (\tau_L + t_{\text{min}})$ , where  $t_{\text{min}} = 60$  fs,  $\tau_L$  is the laser pulse duration, and  $\alpha$  varies linearly from 3 at the intensity  $2 \times 10^{18}$  W/cm<sup>2</sup> to 1.3 at  $3 \times 10^{19}$  W/cm<sup>2</sup> and stays constant at 1.3 for higher intensities.

Table I shows a comparison of calculations of the maximum proton energies  $E_{\text{max/front}}$  and  $E_{\text{max/rear}}$  coming from the front and rear surfaces compared to experiments performed in a wide range of laser and target conditions (in particular for short pulse durations and/or low irradiances that we did not explore experimentally in the previous sections). The revised analytical estimate for RSA is in good agreement with the experimental measurement. Figure 12 shows the predictions of this revised RSA model in the 2D plane of laser intensities and laser pulse duration, for the parameters for which we have confidence the model can be applied. Indeed, we have to note that for thin targets, long laser pulses ( $> 1$  ps) and very high laser intensities ( $> 10^{20}$  W cm<sup>-2</sup>), the analytical model fails and overestimates the produced maximum proton energy. This has been recently shown by Robson *et al.*<sup>72</sup> This is due to the fact that for these conditions, the hot electrons injected in the target by the long pulse leading edge induce preheating of the rear surface of the source foil in the form of a plasma gradient with scale length  $\lambda_s \gg \lambda_D$ , where  $\lambda_D$  is the Debye length of the hot electrons driving the ion acceleration. Therefore, this reduces the strength of the initial driving electric field from  $E_0 = k_B T_{e0} / (e \lambda_D)$ , if there would be no gradient, to  $E_1 = k_B T_{e0} / (e \lambda_s) \ll E_0$ , hampering proton acceleration. Such a reduction to a rear-surface gradient has been recently demonstrated using numerical simulations.<sup>73</sup> The agreement observed in Table I between the model and the measurements for very high laser intensities is due to the fact that the target thickness in those experiments was large (100  $\mu$ m), and therefore the preheat effect mentioned before was minimized as the electrons have diluted traveling through the thick target.

Although we have not taken into account in our calculations a possible boosting of FSA protons by the rear-surface field (if the target is thin enough so that the rear-surface field is still large when these ions cross the rear surface<sup>74</sup>), the good agreement between experimental measurements and RSA estimates suggests that in all cases RSA is predominant in producing the highest energy protons. FSA always give proton energies much lower than RSA. This is also observed in Fig. 13, where we plot, for various laser pulse duration, target thickness, and laser intensity on target the maximum

TABLE I. Comparison of RSA- and FSA-produced maximum proton energy for various experiments. To compute the FSA proton energy, the slowing down in the target of the FSA produced protons is taken into account. Note that in the FSA estimates, we do not take into account a boosting that could take place at the rear surface due to the sheath fields. For laser pulse durations up to 170 fs, the laser wavelength of the reported experiments is  $0.8 \mu\text{m}$ . Otherwise, it is  $1 \mu\text{m}$ . For each calculation, we use the laser focal spot size as given in each reference.

Reference	Intensity ( $\text{W}\cdot\text{cm}^{-2}$ )	Target thickness ( $\mu\text{m}$ )	$\tau_{\text{laser}}$ (fs)	Focal spot FWHM ( $\mu\text{m}$ )	$E_{\text{max}}$ RSA (MeV)	$E_{\text{max}}$ FSA (MeV)	Measured $E_{\text{max}}$ (MeV)
75	$2 \times 10^{19}$	10	40	10	4.5	1	3
49	$6 \times 10^{19}$	6	40	4	9.2	2.5	10
69	$2 \times 10^{18}$	5	55	7	0.47	0	0.5
69	$6 \times 10^{18}$	5	55	7	2	0.4	1.2
76	$7 \times 10^{18}$	5	60	5.2	2	0.5	1.3
68	$2.7 \times 10^{18}$	3	70	7.5	1	0.17	0.88
69	$2 \times 10^{18}$	5	170	7	1.15	0	1.15
61	$4 \times 10^{19}$	20	320	6	21	2.2	20
3	$3 \times 10^{20}$	100	500	9	46	6.3	56
77	$2 \times 10^{20}$	100	700	7	36	4.7	42
61	$10^{19}$	25	800	6	10	0	10.2
61	$2 \times 10^{18}$	25	10000	6	10	0	9.5

proton energies produced by RSA and FSA as given by the analytical estimates. We also observe a predominance of RSA over FSA. This could be reversed for ultrashort pulses ( $<10$  fs) where the laser energy is very low and thus the number of accelerated electrons toward the rear surface is low, reducing, therefore, the strength of the rear-surface accelerating field.

## VI. CONCLUSION

We have established that, for a large range of laser intensities and pulse durations, rear-surface acceleration produces the maximum energy of protons that are accelerated forward by high-intensity, short-pulse lasers from thin metal foils. We have observed this in two laser intensity regimes. For high-intensity [ $(1-6) \times 10^{19} \text{ W cm}^{-2}$ ] and moderately long pulse (300–850 fs) lasers, we observed, when irradiating thin ( $20 \mu\text{m}$ ) metal targets, the production of two distinct proton beams accelerated in the laser forward direction. A low-angle ( $\leq 20^\circ$ ), high-energy ( $>16$  MeV) proton beam originates from the target rear surface through high-field

electrostatic acceleration whereas a large-angle, low-energy ( $\leq 6$  MeV) beam originates from the target front side through the electrostatic field generated by the electron displacement into the target. For protons  $>3.5$  MeV, front-side

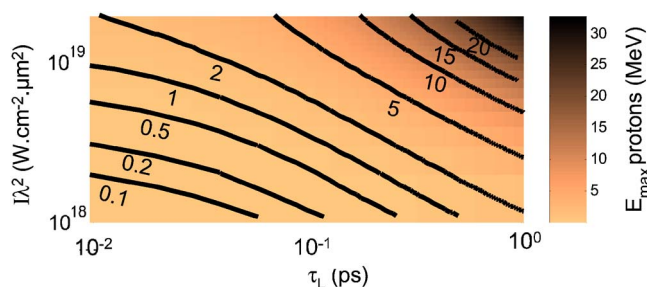


FIG. 12. (Color online) Analytical estimates of RSA-produced maximum proton energy for various laser intensities and pulse duration. The target thickness is  $10 \mu\text{m}$ , the FWHM laser focal spot is  $6 \mu\text{m}$ , and the laser wavelength is  $1 \mu\text{m}$ . The contour lines are for a constant maximum proton energy in units of MeV.

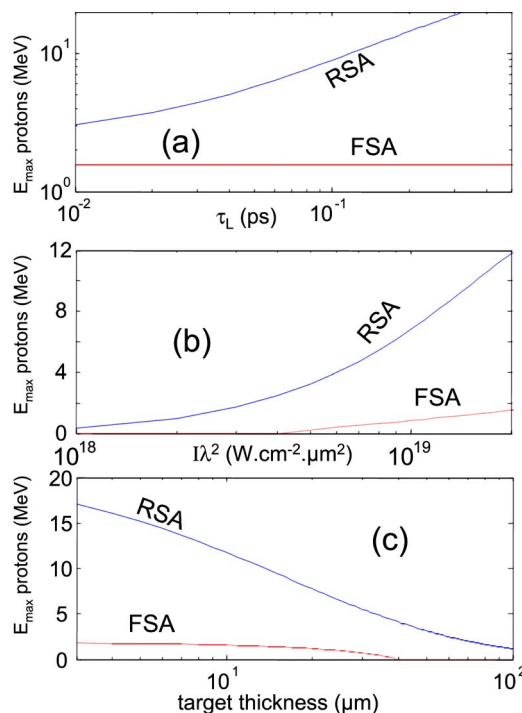


FIG. 13. (Color online) Analytical estimates of RSA- and FSA-produced maximum proton energy for various target and laser parameters. For (a),  $I = 2 \times 10^{19} \text{ W cm}^{-2}$  and the target thickness is  $10 \mu\text{m}$ . For (b), the target thickness is  $10 \mu\text{m}$  and  $\tau_L = 150$  fs. For (c),  $I = 2 \times 10^{19} \text{ W cm}^{-2}$  and  $\tau_L = 150$  fs. To compute the FSA proton energy, the slowing down in the target of the FSA produced protons is taken into account. Note, however, that in the FSA estimates we do not take into account a boosting that could take place at the rear surface due to the sheath fields. For all calculations, a FWHM laser focal spot of  $10 \mu\text{m}$  is assumed. The laser wavelength is assumed to be  $1 \mu\text{m}$ .

acceleration accounts for <3% of the total energy of the accelerated protons. At a lower laser intensity ( $2 \times 10^{18} \text{ W cm}^{-2}$ ), direct proton radiography of the sheath field on the thin target rear surface also shows that the highest energy accelerated protons are accelerated from the target rear surface. In other laser intensity or laser pulse duration regimes we did not explore experimentally, we have compared analytical estimates of the proton energy produced by rear-surface and front-surface acceleration to a wide range of published results. The comparison gives the consistent picture that for thin targets, rear-surface acceleration produces the highest energy protons, even for very short laser pulses (30–60 fs).

It is important to note that when the target thickness is increased, the spread of the hot electrons in the target induces a lower strength for the RSA electrostatic field and thus reduces proton energies, whereas FSA is not affected. For example, we observe that for our laser parameters and for target thicknesses  $>85 \mu\text{m}$ , RSA protons may be reduced to lower energies than the FSA ones.

The collimation and the low emittance of the predominant RSA protons are an important advantage for potential applications that require high-quality beams such as tabletop ion accelerators. FSA protons are divergent and limited to low energies (a few MeV) but could still be useful for future applications such as radioisotope production, which do not require high-quality beams.

## ACKNOWLEDGMENTS

We acknowledge the expert support of the LULI and Trident laser teams and discussions with L. Gremillet, T. Grismayer, and P. Mora.

This work was supported by Grant No. E1127 from Région Ile-de-France, EU program HPRI CT 1999-0052, LANL Laboratory Directed Research & Development, corporate support of General Atomics, and UNR Grant No. DE-FC08-01NV14050.

- <sup>1</sup>M. Borghesi, J. Fuchs, S. V. Bulanov, A. J. Mackinnon, P. Patel, and M. Roth, *Fusion Sci. Technol.* **49**, 412 (2006).
- <sup>2</sup>E. L. Clark, K. Krushelnick, J. R. Davies *et al.*, *Phys. Rev. Lett.* **84**, 670 (2000).
- <sup>3</sup>R. A. Snavely, M. H. Key, S. P. Hatchett *et al.*, *Phys. Rev. Lett.* **85**, 2945 (2000).
- <sup>4</sup>T. Cowan, J. Fuchs, H. Ruhl *et al.*, *Phys. Rev. Lett.* **92**, 204801 (2004).
- <sup>5</sup>M. Borghesi, A. J. Mackinnon, D. H. Campbell, D. G. Hicks, S. Kar, P. K. Patel, D. Price, L. Romagnani, A. Schiavi, and O. Willi, *Phys. Rev. Lett.* **92**, 055003 (2004).
- <sup>6</sup>S. Gitomer, R. Jones, F. Begay, A. Ehler, J. Kephart, and R. Kristal, *Phys. Fluids* **29**, 2679 (1986).
- <sup>7</sup>M. I. K. Santala, M. Zepf, F. N. Beg *et al.*, *Appl. Phys. Lett.* **78**, 19 (2001).
- <sup>8</sup>M. Borghesi, D. H. Campbell, A. Schiavi *et al.*, *Phys. Plasmas* **9**, 2214 (2002).
- <sup>9</sup>M. Roth, A. Blazevic, M. Geissel *et al.*, *Phys. Rev. ST Accel. Beams* **5**, 061002 (2002).
- <sup>10</sup>A. J. Mackinnon, P. K. Patel, M. Borghesi *et al.*, *Phys. Rev. Lett.* **97**, 045001 (2006).
- <sup>11</sup>M. Roth, T. E. Cowan, M. H. Key *et al.*, *Phys. Rev. Lett.* **86**, 436 (2001); M. Temporal, J. J. Honrubia, and S. Atzeni, *Phys. Plasmas* **9**, 3098 (2002); P. Patel, A. J. Mackinnon, M. H. Key, T. E. Cowan, M. E. Foord, M. Allen, D. F. Price, H. Ruhl, P. T. Springer, and R. Stephens, *Phys. Rev. Lett.* **91**, 125004 (2003); G. Maynard and M. D. Barriga-Carrasco, *Nucl. Instrum. Methods Phys. Res. A* **544**, 84 (2005); M. Key, R. Freeman, S.

- Hatchett, A. Mackinnon, P. Patel, R. Snavely, and R. Stephens, *Fusion Sci. Technol.* **49**, 440 (2006); M. Key, K. Akli, F. Beg *et al.*, *J. Phys. IV* **133**, 371 (2006).
- <sup>12</sup>A. Boyer, M. Goitein, T. Lomax, and E. Pedroni, *Phys. Today* **55** (9), 34 (2002); S. Bulanov, T. Zh. Esirkepov, V. S. Khoroshkov, A. V. Kuznetsov, and F. Pegoraro, *Phys. Lett. A* **299**, 240 (2002); C.-M. Ma and R. Maughan, *Med. Phys.* **33**, 571 (2006), and references therein.
- <sup>13</sup>K. Matsukado, T. Esirkepov, K. Kinoshita *et al.*, *Phys. Rev. Lett.* **91**, 215001 (2003); X. Wang, K. Nemoto, T. Nayuki, Y. Oishi, and K. Eidmann, *Phys. Plasmas* **12**, 113101 (2005); L. Willingale, S. P. D. Mangles, P. M. Nilson *et al.*, *Phys. Rev. Lett.* **96**, 245002 (2006).
- <sup>14</sup>D. Neely, P. Foster, A. Robinson *et al.*, *Appl. Phys. Lett.* **89**, 021502 (2006); P. Antici, J. Fuchs, E. d'Humières *et al.*, *Phys. Plasmas* **14**, 030701 (2007).
- <sup>15</sup>J. Denavit, *Phys. Rev. Lett.* **69**, 3052 (1992).
- <sup>16</sup>D. W. Forslund and C. R. Shonk, *Phys. Rev. Lett.* **25**, 1699 (1970).
- <sup>17</sup>S. C. Wilks, W. L. Kruer, M. Tabak, and A. B. Langdon, *Phys. Rev. Lett.* **69**, 1383 (1992).
- <sup>18</sup>Y. Sentoku, T. E. Cowan, A. Kemp, and H. Ruhl, *Phys. Plasmas* **10**, 2009 (2003).
- <sup>19</sup>P. Gibbon, *Phys. Rev. E* **72**, 026411 (2005).
- <sup>20</sup>M. Hegelich, S. Karsch, G. Pretzler *et al.*, *Phys. Rev. Lett.* **89**, 085002 (2002).
- <sup>21</sup>A. J. Kemp, J. Fuchs, Y. Sentoku *et al.*, *Phys. Rev. E* **75**, 056401 (2007).
- <sup>22</sup>K. Nemoto, A. Maksimchuk, S. Banerjee, K. Flippo, G. Mourou, D. Umstadter, and V. Yu. Bychenkov, *Appl. Phys. Lett.* **78**, 595 (2001).
- <sup>23</sup>A. Youssef, R. Kodama, and M. Tampo, *Phys. Plasmas* **13**, 030702 (2006); H. Habara, K. L. Lancaster, S. Karsch *et al.*, *Phys. Rev. E* **70**, 046414 (2004).
- <sup>24</sup>B. M. Hegelich, B. J. Albright, J. Cobble, K. Flippo, S. Letzring, M. Paffett, H. Ruhl, J. Schreiber, R. K. Schulze, and J. C. Fernandez, *Nature* **439**, 441 (2006).
- <sup>25</sup>A. J. McKinnon, M. Borghesi, S. Hatchett, M. H. Key, P. K. Patel, H. Campbell, A. Schiavi, R. Snavely, S. C. Wilks, and O. Willi, *Phys. Rev. Lett.* **86**, 1769 (2001).
- <sup>26</sup>L. Silva, M. Marti, J. R. Davies, R. A. Fonseca, C. Ren, F. S. Tsung, and W. B. Mori, *Phys. Rev. Lett.* **92**, 015002 (2004).
- <sup>27</sup>E. d'Humières, E. Lefebvre, L. Gremillet, and V. Malka, *Phys. Plasmas* **12**, 062704 (2005).
- <sup>28</sup>E. Fourkal, B. Shahine, M. Ding, J. Li, T. Tajima, and C. Ma, *Med. Phys.* **29**, 2788 (2002); Q. Dong, Z.-M. Sheng, M. Y. Yu, and J. Zhang, *Phys. Rev. E* **68**, 026408 (2003); T. Esirkepov, M. Yamagiwa, and T. Tajima, *Phys. Rev. Lett.* **96**, 105001 (2006); L. Yin, B. J. Albright, B. M. Hegelich, and J. C. Fernandez, *Laser Part. Beams* **24**, 291 (2006).
- <sup>29</sup>J. Fuchs, J. C. Adam, F. Amiranoff *et al.*, *Phys. Rev. Lett.* **80**, 2326 (1998).
- <sup>30</sup>Y. Murakami, Y. Kitagawa, Y. Sentoku, M. Mori, R. Kodama, K. A. Tanaka, K. Mima, and T. Yamanaka, *Phys. Plasmas* **8**, 4138 (2001).
- <sup>31</sup>A. Pukhov, *Phys. Rev. Lett.* **86**, 3562 (2001).
- <sup>32</sup>L. Pommier and E. Lefebvre, *Laser Part. Beams* **21**, 573 (2003).
- <sup>33</sup>H. Lee, K. H. Pae, H. Suk, and S. J. Hahn, *Phys. Plasmas* **11**, 1726 (2004).
- <sup>34</sup>S. Karsch, S. Düsterer, H. Schwoerer, F. Ewald, D. Habs, M. Hegelich, G. Pretzler, A. Pukhov, K. Witte, and R. Sauerbrey, *Phys. Rev. Lett.* **91**, 015001 (2003).
- <sup>35</sup>M. Zepf, E. L. Clark, F. N. Beg *et al.*, *Phys. Rev. Lett.* **90**, 064801 (2003).
- <sup>36</sup>M. Manclossi, J. J. Santos, D. Batani, J. Faure, A. Debayle, V. T. Tikhonchuk, and V. Malka, *Phys. Rev. Lett.* **96**, 125002 (2006); S. I. Krasheninnikov, A. V. Kim, B. K. Frolov, and R. Stephens, *Phys. Plasmas* **12**, 073105 (2005).
- <sup>37</sup>J. Fuchs, T. E. Cowan, P. Audebert *et al.*, *Phys. Rev. Lett.* **91**, 255002 (2003).
- <sup>38</sup>M. Kaluza, J. Schreiber, M. I. K. Santala, G. D. Tsakiris, K. Eidmann, J. Meyer-ter-Vehn, and K. J. Witte, *Phys. Rev. Lett.* **93**, 045003 (2004).
- <sup>39</sup>T. Lin, K. Flippo, M. Rever, A. Maksimchuk, and D. Umstadter, "Mechanism and control of high-intensity-laser-driven proton acceleration," *Proceedings of the Advanced Accelerator Concepts Conference, Stony Brook, 2004*, AIP Conf. Proc. No. 737 (American Institute of Physics, Melville, NY, 2004), pp. 595–601.
- <sup>40</sup>M. Allen, P. K. Patel, A. Mackinnon, D. Price, S. Wilks, and E. Morse, *Phys. Rev. Lett.* **93**, 265004 (2004).
- <sup>41</sup>J. Fuchs, Y. Sentoku, S. Karsch *et al.*, *Phys. Rev. Lett.* **94**, 045004 (2005).
- <sup>42</sup>D. Strickland and G. Mourou, *Opt. Commun.* **56**, 219 (1985).

- <sup>43</sup>B. Wattellier, J. Fuchs, J. P. Zou, K. Abdeli, and H. Pépin, and C. Haefner, *Opt. Lett.* **29**, 2494 (2004).
- <sup>44</sup>M. Roth, T. E. Cowan, J. C. Gauthier *et al.*, "Intense ion beams accelerated by relativistic laser plasmas," *SPIE Proceedings Charged Particle Detection, Diagnostics, and Imaging (San Diego, 2001)*, edited by O. Delage, E. Munro, and J. Rouse (SPIE, Bellingham, 2001), Vol. 4510, pp. 52–57.
- <sup>45</sup>Y. Sentoku, K. Mima, S. Kojima, and H. Ruhl, *Phys. Plasmas* **7**, 689 (2000); Y. Sentoku, K. Mima, Z. M. Sheng, P. Kaw, K. Nishihara, and K. Nishikawa, *Phys. Rev. E* **65**, 046408 (2002).
- <sup>46</sup>Y. Sentoku, K. Mima, P. Kaw, and K. Nishikawa, *Phys. Rev. Lett.* **90**, 155001 (2003).
- <sup>47</sup>A. Kemp, Y. Sentoku, T. Cowan, J. Fuchs, and H. Ruhl, *Phys. Plasmas* **11**, 5648 (2004).
- <sup>48</sup>Q. L. Dong and J. Zhang, *Phys. Plasmas* **8**, 1025 (2001); Th. Schlegel, S. Bastiani, L. Grémillet, J.-P. Geindre, P. Audebert, J.-C. Gauthier, E. Lefebvre, G. Bonnaud, and J. Delettrez, *Phys. Rev. E* **60**, 2209 (1999); A. Mackinnon, Y. Sentoku, P. K. Patel, D. W. Price, S. Hatchett, M. H. Key, C. Andersen, R. Snavely, and R. R. Freeman, *Phys. Rev. Lett.* **88**, 215006 (2002); M. Allen, Y. Sentoku, P. Audebert *et al.*, *Phys. Plasmas* **10**, 3283 (2003); H. Ruhl, T. Cowan, J. Fuchs, *ibid.* **11**, L17 (2004); A. S. Sandhu, A. K. Dharmadhikari, P. P. Rajeev, G. R. Kumar, S. Sengupta, A. Das, and P. K. Kaw, *Phys. Rev. Lett.* **89**, 225002 (2002); B. M. Hegelich, B. Albright, P. Audebert *et al.*, *Phys. Plasmas* **12**, 056314 (2005); A. Kemp and H. Ruhl, *ibid.* **12**, 033105 (2005); R. Jung, J. Osterholz, K. Löwenbrück *et al.*, *Phys. Rev. Lett.* **94**, 195001 (2005); Z. Chen, G. R. Kumar, Z. M. Sheng, T. Matsuoka, Y. Sentoku, M. Tampo, K. A. Tanaka, T. Tsutsumi, T. Yabuuchi, and R. Kodama, *ibid.* **96**, 084802 (2006).
- <sup>49</sup>S. Fritzler, V. Malka, G. Grillon, J. P. Rousseau, F. Burgy, E. Lefebvre, E. d'Humières, P. McKenna, and K. W. D. Ledingham, *Appl. Phys. Lett.* **83**, 3039 (2003).
- <sup>50</sup>When the hydrogenous layer is directly on an Al target, RSA will not be significantly affected, which we confirmed by comparing the simulated RSA E-fields for targets with  $Z=1$  or 10.
- <sup>51</sup>N. V. Klassen, L. van der Zwan, and J. Cygler, *Med. Phys.* **24**, 1924 (1997).
- <sup>52</sup>[http://www.ispcorp.com/products/dosimetry/content/products/gafchromic/810\\_200/consepefo.html](http://www.ispcorp.com/products/dosimetry/content/products/gafchromic/810_200/consepefo.html).
- <sup>53</sup>H. Habara, R. Kodama, Y. Sentoku, N. Izumi, Y. Kitagawa, K. A. Tanaka, K. Mima, and T. Yamanaka, *Phys. Plasmas* **10**, 3712 (2003).
- <sup>54</sup>J. F. Ziegler, J. P. Biersack, and U. Littmark, *The Stopping and Range of Ions in Solids* (Pergamon, New York, 1996).
- <sup>55</sup>M. Firouzbakht, D. Schlyer, and A. Wolf, *Nucl. Med. Biol.* **25**, 161 (1998).
- <sup>56</sup>P. Mora, *Phys. Rev. Lett.* **90**, 185002 (2003).
- <sup>57</sup>A. Youssef, R. Kodama, H. Habara, K. A. Tanaka, Y. Sentoku, M. Tampo, and Y. Toyama, *Phys. Plasmas* **12**, 110703 (2005).
- <sup>58</sup>E. Lefebvre and G. Bonnaud, *Phys. Rev. E* **55**, 1011 (1997).
- <sup>59</sup>The target for this PIC simulation is modified so that, as in the experiment, there sits on the target rear surface a  $0.5 \mu\text{m}$   $\text{CD}_2$  layer [i.e.,  $\text{D}^+(50\%)$ ,  $\text{C}^{4+}(25\%)$ ,  $\text{C}^{3+}(25\%)$ ] (Ref. 20)] covered by the same contaminants.
- <sup>60</sup>J. H. Gibbons and R. L. Macklin, *Phys. Rev.* **114**, 571 (1959); R. E. Segel, S. S. Hanna, and R. G. Allas, *ibid.* **139**, B818 (1965).
- <sup>61</sup>J. Fuchs, P. Antici, E. d'Humières *et al.*, *Nat. Phys.* **2**, 48 (2006).
- <sup>62</sup>M. Borghesi, S. Bulanov, D. H. Campbell *et al.*, *Phys. Rev. Lett.* **88**, 135002 (2002).
- <sup>63</sup>H. Ruhl, T. Cowan, and J. Fuchs, *Phys. Plasmas* **11**, L17 (2004).
- <sup>64</sup>L. Romagnani, J. Fuchs, M. Borghesi *et al.*, *Phys. Rev. Lett.* **95**, 195001 (2005).
- <sup>65</sup>T. Takizuka and H. Abe, *J. Comput. Phys.* **25**, 205 (1977).
- <sup>66</sup>Y. Sentoku, K. Mima, Y. Kishimoto, and M. Honda, *J. Phys. Soc. Jpn.* **67**, 4084 (1998).
- <sup>67</sup>K. Nambu and S. Yonemura, *J. Comput. Phys.* **145**, 639 (1998); Y. T. Lee and R. M. More, *Phys. Fluids* **27**, 1273 (1984).
- <sup>68</sup>A. Fukumi, M. Nishiuchi, H. Daido *et al.*, *Phys. Plasmas* **12**, 100701 (2005).
- <sup>69</sup>Y. Oishi, T. Nayuki, T. Fujii *et al.*, *Phys. Plasmas* **12**, 073102 (2005).
- <sup>70</sup>J. Fuchs, J. C. Adam, F. Amiranoff *et al.*, *Phys. Plasmas* **6**, 2569 (1999), and references therein.
- <sup>71</sup>E. d'Humières, J. Fuchs, P. Antici *et al.*, *Plasma Phys. Controlled Fusion* (submitted).
- <sup>72</sup>L. Robson, P. T. Simpson, R. J. Clarke *et al.*, *Nat. Phys.* **3**, 58 (2007).
- <sup>73</sup>T. Grismayer and P. Mora, *Phys. Plasmas* **13**, 032103 (2006).
- <sup>74</sup>P. Gibbon, F. N. Beg, E. L. Clark, R. G. Evans, and M. Zepf, *Phys. Plasmas* **11**, 4032 (2004).
- <sup>75</sup>J. Schreiber, S. Ter-Avetisyan, E. Risse, M. P. Kalachnikov, P. V. Nickles, W. Sandner, U. Schramm, D. Habs, J. Witte, and M. Schnürer, *Phys. Plasmas* **13**, 033111 (2006).
- <sup>76</sup>T. Fujii, Y. Oishi, T. Nayuki *et al.*, *Appl. Phys. Lett.* **83**, 1524 (2003).
- <sup>77</sup>P. McKenna, K. W. D. Ledingham, J. M. Yang *et al.*, *Phys. Rev. E* **70**, 036405 (2004).
- <sup>78</sup>R. Ramis, R. Schmalz, and J. Meyer-ter-Vehn, *Comput. Phys. Commun.* **49**, 475 (1988).